JOURNAL OF SPACECRAFT AND ROCKETS
Vol. 33, No. 3, May–June 1996

Optical Radiations from Interaction of Effluent Gases with the Low-Orbital Atmosphere

David L. A. Rall* and Irving L. Kofsky*
PhotoMetrics, Inc., Woburn, Massachusetts 01801-2067
Charles P. Pike† and David J. Knecht‡
U.S. Air Force Phillips Laboratory, Hanscom Air Force Base, Massachusetts 01731-3010
and
Theodore P. Zehnpfennig§
Visidyne, Inc., Burlington, Massachusetts 01803-4512

The radiance distributions of the short-wavelength infrared and visible glows associated with interaction of exhaust from Shuttle orbiter's primary reaction control system thrusters with background air are interpreted as resulting from independent kinetic processes involving major and fuel-fragment components of the hypervelocity combustion gas. These luminous volumes become essentially stable in the spacecraft's moving reference frame by 1 s after the engine's liquid bipropellant ignites, with dimensions on the order of kilometers. Viewed perpendicular to the vehicle trajectory, they have Gaussian brightness profiles in ram and, at visible wavelengths, an edge-enhanced ogival shape in wake injections. Strong vibrational emission arises from collisions of water molecules, which also emit over a broad infrared range when outgassed from low-orbiting spacecraft. Other phenomenological features of these optical-contaminant glows quantified from ground-based radiometric images include 1) total exoatmospheric photon yields, 2) volume emission rates and downstream movement of the surface brightness maxima as the ambient reactant species becomes depleted, and 3) cross sections for quenching the luminosity. The absolute visible-band intensities from three exhaust directions indicate a potential barrier for the excitative reactions, and with the patterns of projected radiance apply in remote sensing of angles between the thrust axis and the spacecraft velocity.

Nomenclature

A, B = number of precursor radiating molecules or atoms
c_A, c_B = total rates of species reactions, s^{-1}
J = molecular rotational quantum number
t = time after initiation of thruster engine firing, s
V = velocity of advance, km s^{-1}
v, v_{1-3} = molecular vibrational quantum numbers
x = distance, km
τ, τ_{1-3} = characteristic reaction times, s

Introduction

VISIBLE radiations excited by the combustion products of the Space Shuttle's primary reaction control system (PRCS) thruster motors have been found[1] to originate from up to several kilometers into the low-Earth-orbital atmosphere, and to increase in intensity with increasing energy of collision with the background air. This interaction volume can be associated with the diffusive-expansion phase[2] of the exhaust gases; its decrease in brightness toward the engine nozzles is attributed to depletion of ambient gas in the continuum-flow region.[3–5] As the initial translational energy of molecules desorbed and vented from spacecraft moving at ≈7.8 km s^{-1} relative to the thermosphere is of the same order as those from thrusters (typically 3.5 km s^{-1}), their impacts on local air also result in internal excitations. The flowfield of these effluents underlies the optical (foreground-clutter) and physical (impingement, mass-redeposition) contamination commonly found to degrade space operations.

The primary direct source of data on exhaust–atmosphere interactions are ground-based radiometric images[1] and spectra[6] in the visible–near-uv, and images in the short-wavelength infrared.[7] In addition, visible–uv spectra from onboard of liquid-bipropellant combustion gas identify some of its potentially reactive minor components.[8] Related laboratory studies include those of hyperthermal ion–neutral reactions,[9,10] which excite both visible[6] and infrared[10,11] emissions, and of impacts of orbital-velocity oxygen atoms on known and putative exhaust molecules.[12–17] Further support is provided by the older combustion literature referenced below, and recent spectroradiometry of outgas and optically active species released from orbiter.[18] The field experiments are interpreted with the aid of a Monte Carlo flowfield model[19] that predicts the emission rates of rovibrational features and their transmission to endoatmospheric sensors. The purpose of this report is to apply this information to understanding the optical excitation by, and transport of, PRCS engine exhaust and other effluents in the near-space environment.

Ground-Based Measurements

General

This review is given scope by the above-mentioned spectroradiometric data, which we obtained using large-aperture, precisely tracking telescopes at the Air Force Maui Optical Site[20] (AMOS) atop 3050-m Mt. Haleakala, Hawaii. Parallel-oriented pairs of the 870-lb-thrust PRCS engines [monomethyl hydrazine (MMH) fuel, nitrogen tetroxide oxidizer] were operated near culmination to provide views about perpendicular to Shuttle orbiter's trajectory during overpasses of STS-56, -33, -38, and -41. In a typical experiment these attitude-controlling thrusters were fired sequentially into ram, into wake, and perpendicular to track toward the zenith and then nadir for closely 3-s periods; at STS-56, a longer-duration ram burn was imaged. The foreoptics of the specially built imaging spectrograph[21] was designed to encompass the full visible–near-uv interaction volume.

The surface brightnesses of these regions lead immediately to their total photon yields. When the axis of the exhaust stream is

---

Received April 13, 1995; revision received Nov. 21, 1995; accepted for publication Nov. 27, 1995.

*Staff Scientist, 4 Arrow Drive.

†Supervisory Physicist, Spacecraft Interactions Branch (WSAI), 29 Randolph Road.

‡Physicist, Spacecraft Interactions Branch.

§Engineer, 99 South Bedford Street.

within a few degrees of direct ram or wake, the near-cylindrical symmetry of these brightnesses allows them to be straightforwardly unfolded to derive distributions of the volume emission rate. This more fundamental quantity depends on the local densities of injected and background gases, the rate coefficients for exciting and collisionally deactivating radiative species, and their upper-state lifetimes and branching ratios. The volume emission rates are subject to effects of diffusion, as will become apparent later. Interpretation of the images is complicated by the large number of atoms and molecules that may be emitting within the typically broad spectrum intervals of the cameras, as well as of nonradiative species that can take part in precursor and/or quenching reactions.

The brightness distributions and total optical power outputs are sufficiently different to apply to determining thrust angles of engine firings on noncooperating spacecraft. The dependence of radiant intensity on time after ignition indicates the order of the processes producing visible and infrared photons, a principal finding of the experiments reviewed here. Glow that persists after thruster shutdown conveys further chemistry and dynamics information, including rates of impact of particles in the interaction region on the Shuttle orbiter's body.[6]

Imagers

The video cameras imaged onto intensified silicon intensifier target photocathodes having S-20R spectral response (0.39–0.67 μm FWHM, including lens transmissions). We took the output currents over dark baseline to be proportional to the spatially corresponding irradiances at these cameras' focal planes, as when analyzing their photographs of other thermospheric emission and sunlight-scattering events.[22–24] This assumption of linear response introduces only small photometry error relative to other sources of inaccuracy when these currents are below about $\frac{3}{4}$ of saturation. The photocurrent distributions were accessed and (where indicated) coadded and baseline-suppressed using standard digital image-processing hardware, and converted to numerical descriptors using largely proprietary software. The absolute response was calibrated against the tabulated[25] irradiances produced by known stars, whose angular separations provided an accurate transverse distance scale at orbiter's ranges from AMOS.

The infrared camera photographed a ram glow produced on mission STS-56 with the aid of a specially designed 40-cm-aperture auxiliary telescope. Its focal-plane detector is a liquid-nitrogen-cooled 128 × 128 element indium antimonide array, which was read out each 0.14 s. Figure 1 shows the transmission of its prefilter and of the low-latitude maritime-atmosphere sight path above the mountaintop station, calculated using 5-cm^{-1}-spectral-resolution LOWTRAN, along with the spectral locations of vibrational features currently favored. The actual attenuations of these rotationally broadened bands call for the line-by-line calculations noted later; these attenuations were found to depend only weakly on the humidity profile of the troposphere over the range accompanying visually clear nights at AMOS.

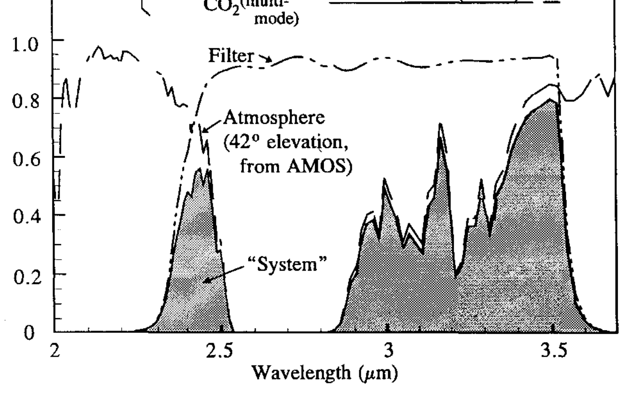

Fig. 1 Transmissions of the InSb-photocathode camera filter and the atmosphere at STS-56 culmination.

The quantum conversion efficiency of InSb remains nearly constant in the wavelength interval of Fig. 1. Thus the product of these two transmissions, indicated by shading, is the relative response of this imaging system to exoatmospheric radiation sources (at 5-cm^{-1} resolution). As with the visible-light signal, we digitized the photocurrents above thermal leakage baseline to determine the relative scene brightnesses in the short-wavelength infrared (SWIR) interval. The absolute radiometric sensitivity applied is based on extrapolation of a stellar calibration at a somewhat shorter wavelength.

PRCS Exhaust

Mole fractions of the major exhaust products averaged over the exit plane are calculated to be 0.33 H_2O, 0.31 N_2, 0.16 H_2 and 0.03 H, and 0.13 CO and 0.042 CO_2.[9,26,27] Minor (0.1–1% mole fraction) and trace (<0.1%) species, originating largely from zones having other than the mean temperature and oxidizer/fuel ratio in the combustion chamber, are present in as yet unquantified concentrations. (These concentrations presumably vary with time after ignition, and also with streamline location, as an excess liquid-fuel film cools the chamber walls.[8]) Among these species are low-molecular-weight hydrocarbons, such as acetylene, whose reactions are considered to be the source of most of the electronic emissions from the interaction volumes. The minor components include raw MMH both as vapor and as droplets, MMH pyrolysis fragments, and NO. Trace NO_2, CN, CH, CH_2, C_2, and HNO have been identified[8,27] from firings of PRCS and smaller-scale MMH–N_2O_4 rocket motors.

Background on Excitative Reactions

To aid in interpreting the images of the glows excited by these molecules, we briefly review the relevant emission spectra and cross sections that have recently emerged. As is shown later, the vibrational (SWIR) emission rates, unlike the visible–uv, are much too high to be explained by processes involving minor exhaust components. We introduce here the perceivedly important luminosity-producing reactions of major components, and assess their contribution in connection with our analysis of the AMOS and supporting data.

Water Vapor

H_2O is a particularly ubiquitous spacecraft-environment contaminant. Besides constituting one-third of liquid-bipropellant exhaust, water molecules are continuously outgassed from exposed surfaces and intermittently flash-evaporated as part of stationkeeping, both directly[26] and from ventings of liquid.[22] Rates of production of H_2O vapor from these sources during Space Shuttle operations are 400 g s^{-1} per individual PRCS engine[9]; roughly 0.02 g s^{-1}, the exact figure depending strongly upon presoak conditions and time since launch[28,29]; and of order 20 g s^{-1} when steam is released[26] and 2 g s^{-1} from standard dumps of excess water.[22] Gas is evaporated and sublimed from these liquid streams and the particles into which they fragment, primarily in the initial ≈5 m from orbiter, and thus also becomes nearly isotropic around its body.[30]

The average center-of-mass energy in first collisions of ram-directed PRCS exhaust H_2O with the principal orbital-altitude species O is just below 6 eV. When these molecules desorb (in which case no continuum-flow phase develops) or arise from flash evaporations, almost 3 eV is available. These translational energies exceed the excitation thresholds of a large number of vibrational and pure rotational states of H_2O and OH. [H_2O^+ can also be produced, by impact on ionospheric $O^+(^4S)$; the charge-exchange reactions also populate at least one electronic state of neutral oxygen.[6]] In consequence, considerable interest has developed in hypervelocity water-vapor-associated excitation.[11,16,17,19,28,30–34] Nonetheless the experimental database remains sparse—the two stretch-mode fundamental bands (100 and 001 → 000) have not been spectrally resolved from one another, for example—and the theoretical state-to-state cross sections differ among themselves.[11] Most recently, infrared foregrounds from outgas have appeared within the fields of view of orbiter spectroradiometers,[35–37] which besides identifying the principal transitions lead to the idea that the 2–3-order-of-magnitude-higher signal from purposely released water, unobscured by still-hot combustion products, would further aid in investigating exhausted-water collisions.

H_2O has in fact been found to be responsible for most—on unpowered space vehicles perhaps all—of the gaseous foreground contaminating geophysical data from infrared sensors. Its radiations are in part due to its initial thermal population[28,31] and pumping by sunlight or earthshine.[11,30] For most optical configurations, however, they come primarily from its several internal-excitation-producing reactions with background oxygen atoms.[11,19,37] (Rates of excitation of SWIR by collisions on the less-abundant nitrogen molecules are several orders of magnitude lower.[14]) After the departing water molecules have relaxed radiatively, the principal such single-step processes are considered to be

$$\mathrm{H_2O}(\tilde{X}, 000) + \mathrm{O}(^3P)$$
$$\rightarrow \begin{cases} \mathrm{H_2O}(\tilde{X}, 100, 010, 001\ [\text{principally}], \\ \quad 020, 011, 111, \ldots) + \mathrm{O}(^3P) & \text{(1a)} \\ \mathrm{H_2O}(\tilde{X}, \nu_1\nu_2\nu_3 \geq 0, J \gg 0) + \mathrm{O}(^3P) & \text{(1b)} \\ \mathrm{OH}(X^2\Pi, v > 0) + \mathrm{OH}(X) & \text{(1c)} \end{cases}$$

and to a lesser extent

$$\mathrm{H_2O}(\tilde{X}, 000) + \mathrm{O}^+(^4S)$$
$$\rightarrow \mathrm{H_2O}(\tilde{X}^2B_1, 001, 100, 010, 012, 111, 020, \ldots) + \mathrm{O}(^3P) \tag{2}$$

The resulting optical emissions, in rough order of intensity, are primarily as follows:

1) Spectrally widespread pure-rotation lines of neutral H_2O, with about equal energy yields in the wavelength intervals[31] 5–16, 17–22, and 23–28 μm.

2) The commonly encountered fundamental bending (ν_2) and stretching (ν_1, ν_3) mode sequences of H_2O, rotationally broadened around 6.3 and 2.7 μm.

3) The fundamental and first-overtone rovibrational cascade[11,19] from OH (vibrationally excited) longward of 2.8 and 1.3 μm.

4) Multiquantum and multimode (combination) bands[11] of H_2O, and also H_2O^+, principally near 1.9, 3.1, and 4.7 μm.

5) Stretch- and bending-mode fundamental bands[11] of H_2O^+ near 3 and 7 μm (the partial cross sections for internal excitation of this product of hyperthermal charge exchange are large[9,10]).

The high-resolution 4–22-μm spectra of outgas recently obtained by viewing from orbiter,[36,37] although outside the response interval of the AMOS infrared camera, contain particularly relevant information. Their vibrational development[37] near 6.3 μm indicates that little H_2O ν_2 emission extends down to these wavelengths, and furthermore, shows no evidence of H_2O^+ ν_2. The undetectability of pure-rotation lines of OH against the strong, spectrally dense lines from H_2O means that relatively few hydroxyl radicals are produced in high rotational states at 3-eV center-of-mass collision energy.

The H_2O ν_2 emission between 5 and 6 μm seen by the cryocooled Fourier-transform spectrometer[37] was obscured by the 1, 0 vibrational band of NO. From its column emission rate and spectral profile, this feature may be interpreted as being the natural (far-field) excitative oxygen atom-exchange radiation predicted by Earth-limb models.[38] That is, the data from this high-performance sensor do not identify nitric oxide as an optically contaminating effluent, nor do they show any other molecular radiations. (Unfortunately, it was not scheduled to operate during control thruster firings or water releases.)

Other Major Combustion Species

Other major components of PRCS exhaust are energetically able to contribute to the SWIR signal, through exothermic reactions with ramming oxygen atoms such as

$$\mathrm{CO}, \mathrm{CO_2} + \mathrm{O}(^3P)$$
$$\rightarrow \mathrm{CO}(X^1\Sigma^+, v \geq 2), \mathrm{CO_2}(\nu_1\nu_2\nu_3 > 0) + \mathrm{O}, \mathrm{O_2} \tag{3}$$

$$\mathrm{N_2}(X) + \mathrm{O}(^3P) \rightarrow \mathrm{NO}\big(X^2\Pi_r, v \geq 2\big) + \mathrm{N} \tag{4}$$

and

$$\mathrm{H_2}(X, v \geq 0) + \mathrm{O}(^3P) \rightarrow \mathrm{OH}(X^2\Pi, v = 1\ \text{or}\ 2) + \mathrm{H} \tag{5}$$

The spectral ranges of the resulting vibrational features, including those of the expectedly weak combination bands of CO_2, are illustrated in Fig. 1. Vibrational emission from carbon monoxide would arise about equally from collisions[15,17] of CO and CO_2; laboratory data indicate that the 4.7-μm CO fundamental would be much stronger than the 4.3-μm CO_2 001 → 000. An on-orbit release of N_2 gas[18] led to an upper limit (10^{-17} cm^2) to the cross section for producing $NO^{\dagger}$, whose overtone sequence lies within the infrared camera's spectral range. The cross sections for the almost thermoneutral reaction (5), though not measured, have been predicted theoretically.[39–41] As noted, we consider these candidate excitative reactions further in our interpretation of the SWIR emission yields.

Electronic Excitation

By contrast, existing data indicate that most of the visible and (particularly) uv from the interaction volumes originates with minor or trace exhaust gases, rather than from conversion of some of the kinetic energy of major combustion species into internal energy of their reaction products. AMOS imaging spectra[6,42] of ram and perpendicular-to-trajectory PRCS exhaust interactions from 290-km-altitude STS-41 and STS-38 showed the following features: 1) NH $A^3\Pi \rightarrow X^3\Sigma$ $\Delta v = 0$ sequence Q branches centered at 3365 Å, which have also been observed spectroscopically from onboard the orbiter[43]; 2) a so far unidentified pseudocontinuum (or unresolved discrete emissions) extending between approximately 3500 and 5000 Å, which represents the major fraction of the signal in the S-20R response range; 3) the O I $^1D \rightarrow {^3P}$ forbidden red doublet at 6300 and 6364 Å, with intensities that would produce only a small fraction of this signal; and 4) weak, spectrally unstructured emission extending longward of 5000 Å.

The NH-radical bands (item 1) lie at wavelengths too short to produce measurable photocurrent from the AMOS video cameras. Their ready excitation, however, highlights the contribution of low-concentration exhaust products, since it does not result from any plausible single reaction or chain starting with the major components. The total yield of these photons from 3-s-duration firings into ram from STS-33 was found to be only a few hundredths percent of the number of PRCS fuel molecules consumed,[42] consistent with the estimated mixing ratios of trace exhaust species. Identification of NH emission gives credence to interpreting the strong blue-green radiation (item 2) as being due to one or more of the other features identified in laboratory combustion of hydrazine and amine compounds, or in hydrocarbon flames[44,45]; these include electronic bands originating from low-lying upper states of C_2, CN, CO, and CH.

The red lines (item 3) originate from only 1.97 eV above the ground state of atomic oxygen, and are well known to be excited by several aeronomic reactions. From exhaust, they have been interpreted[6] as due primarily to nonadiabatic impacts of high-translational-energy H_2O (and also knocked-on ambient oxygen atoms) on $O(^3P)$. A potential second source is excitative charge transfers from H_2O to the principal ionospheric component $O^+(^4S)$, i.e., partitioning of the exothermicity of the reaction (2) into an electronic rather than vibrational states. The analysis indicated that all but a few percent of the metastable $O(^1D)$ atoms are deactivated by further collisions, on exhaust molecules as well as the O and N_2 naturally present. A large fraction of such quenchings by H_2 and H_2O would result in OH radicals, whose third vibrational state is energetically accessible even when the participants have been thermalized; the product hydroxyl could emit only SWIR photons.

Excitation of $O(^1D)$ that would accompany water outgassing or releases has been below sensor threshold in the several surveys of the atmosphere's limb from onboard spacecraft. In addition the O I forbidden green line, which originates from a state (^1S) of the same electronic configuration that lies only 2.2 eV above $O(^1D)$ and furthermore has an about 200 times shorter radiative lifetime, was (curiously) absent in these AMOS spectra.[6] They also show no evidence of near-uv electronic ($A^2\Sigma^+ \rightarrow X\,^2\Pi$) bands of OH.

The weak yellow–red radiation (item 4) gave no spectral indication of being the energetically accessible $\Delta v = 4$ and 5 vibrational sequences of OH formed by impact of exhaust H_2O on background $O(^3P)$, which had been previously anticipated.[1,42] (This observation is consistent with the modest vibrational temperature of reaction-product hydroxyl mentioned later.) Additionally, the mixing ratios of nitric oxide in PRCS exhaust or from later reactions are predicted to be low, and the time scale for excitative two-body recombinations of NO with O is very long compared with that of the observed decay of visible emission from exhaust interactions ($\sim$1-s exponential, as stated below); thus the yellow–red component of the AMOS spectrum would not be the familiar pseudocontinuum from NO_2^*.

Images of the Interaction Volumes

Overview

Representative exposure-contoured AMOS photographs of the glows produced by pairs of parallel-directed PRCS rocket motors are reproduced in Figs. 2a–2d. The plate scales refer to the plane perpendicular to the camera line of sight at the range to orbiter. The vehicle has moved in the direction shown by star tracks about 0.25 km between single video frames, and 1 km in the four-frame averages. Reflection density scales differ among these reproductions of the electronic images, which are the source of the numerical photometry and photogrammetry results to be presented.

Figure 2a compares the radiation patterns at S-20R and SWIR (Fig. 1) wavelengths from a windward-directed firing from STS-56 on Orbit 114. They expanded very slowly beyond the initial 2 s after ignition shown. (Blockage of the tracking telescope's view by its housing precluded observation of engine shutoff some 10 s later.) Orbiter is at 293-km altitude, at 42-deg elevation from AMOS. The exhaust axis is 1.8 deg in depression and 11.8 deg in azimuth (northeast) from the trajectory vector; the trajectory aspect increases from 75 to 76.5 deg and the exhaust-axis aspect from 77 to 79 deg during the data sequence. Radiances are shown with the same arithmetic separation for both cameras, and the times refer to the ends of the exposures. The mean translational energy in the rest frame of (for example) axially directed H_2O and O is 5.8 eV, and for CO_2 and O it is 6.9 eV.

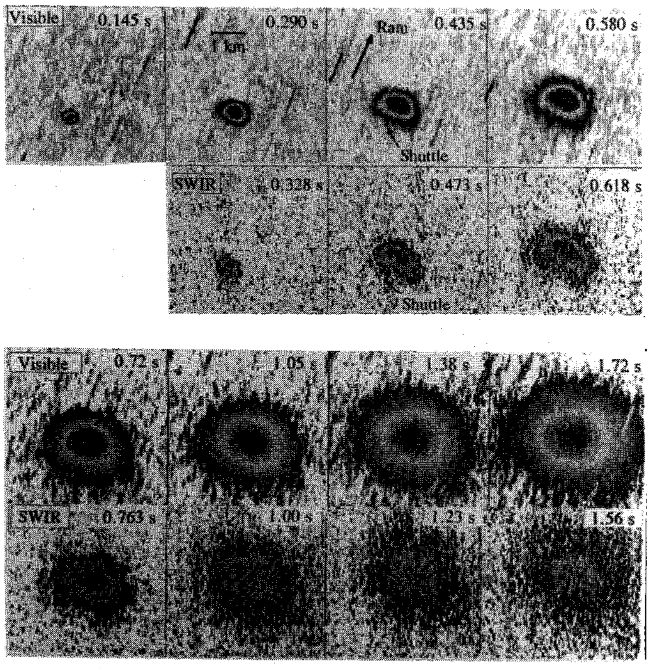

Fig. 2a Ram exhaust interaction from STS-56.

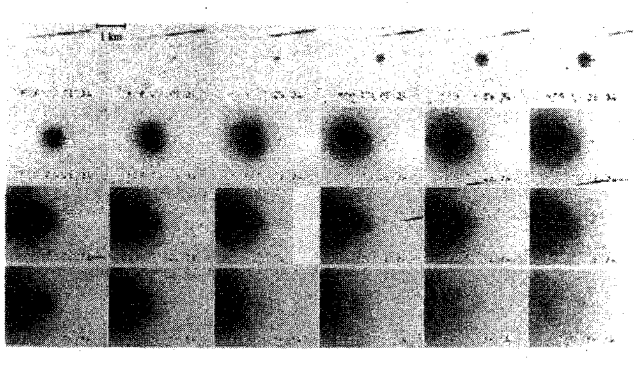

Fig. 2b Ram visible exhaust interaction from STS-33.

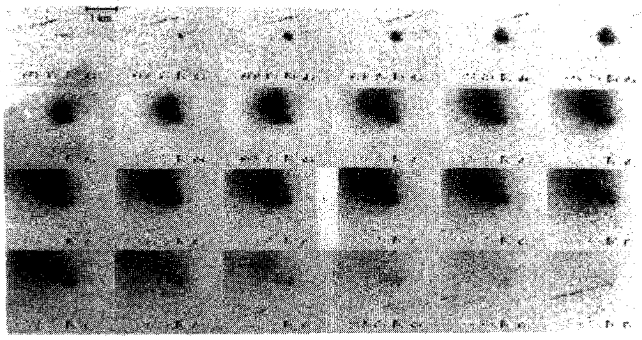

Fig. 2c Perpendicular-to-track visible exhaust interaction from STS-33.

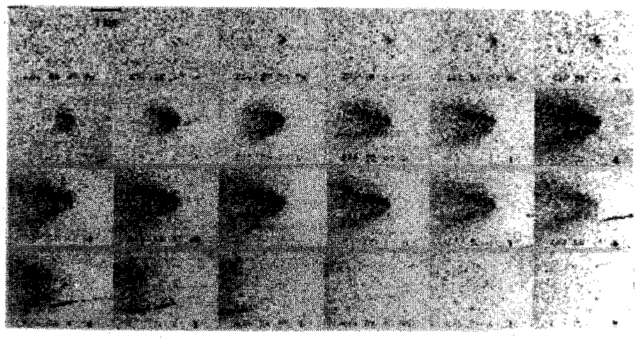

Fig. 2d Wake visible exhaust interaction from STS-33.

Figure 2b is from a video camera whose narrower field encompassed about half of the fully developed STS-33 (orbit 21) ram volume. Its top row reproduces the first six $\frac{1}{30}$-s frames, and subsequent rows are averages of four consecutive frames, with 42–92 (1.40–3.07 s) omitted starting at the middle of the third row as indicated by the gap. The orbiter is at 316-km altitude, 34-deg elevation. The trajectory aspect increases from 68 to 72 deg, and the gray-scale contours are again linearly separated. Detectable visible glow, some of it in the moving spacecraft's retrograde hemisphere, persists for at least 4 s after a nominally 3-s thruster operation. (The engines were turned on and off manually from onboard, uncorrelated with the ground-based camera's framing.)

Figures 2c and 2d are S-20R radiance distributions with exhaust from STS-33 (orbit 21) directed toward the zenith perpendicular to its orbital path and into its wake. The frame timing and averaging are as for Fig. 2b. In Fig. 2c the orbiter is at 319-km, 34-deg elevation, and has trajectory aspect 88–92.5 deg; in Fig. 2d, 320 km, 28 deg, and 79–83 deg. In the retrograde firing, where the average H_2O–O kinetic energy is just under 0.5 eV, the absolute brightnesses and total light yields were found to be one to two orders of magnitude lower than in the normal-to-trajectory (3.2 eV) and posigrade firings.[1]

Ram and Normal-to-Track Exhaust

The ram glows (Figs. 2a and 2b) extend into the forward hemisphere (only) from orbiter, whose location is indicated by a low-contrast patch a few pixels in width (close to the nominal camera resolution). The finger extending from the thrusters in the first few frames from STS-33 becomes about 30 m wide and 200 m axially; a similar, but less pronounced, local structure can also be detected in the STS-56 video images. (Accuracy of the optical measurements is insufficient for meaningful scaling between air densities at the two exhaust-injection altitudes.) By the ninth video frame (0.3 s), a gap some 200 m long has developed between the spacecraft and the volume radiating above camera threshold. This weakening of column emission rates approaching the exhaust exit plane is due to depletion of the ambient chemiluminescent-reaction partner predicted by both classical explosion theory[3,4] and numerical models of the flowfield.[5,19] No further spatial structuring, such as has been seen accompanying the usual ~10-Hz pulsed operation of the control thrusters,[42] is apparent in either the visible-light or the SWIR photographs of the STS-56 interaction.

The perpendicular-to-track visible glow volume (Fig. 2c) streams backward in the orbiter's reference frame, presumably because of the delay in excitation that we identify later. As a consequence, the projected radiances peak at larger angles from the velocity vector of the spacecraft than would be predicted from this velocity and that of the exhausted gas. (The component of the symmetry axis of the initial flow out of the image plane also has the effect of increasing this angle.) The surface brightnesses extending into the retrograde hemisphere have steeper gradients than at the leading edge of the glow, as is shown more quantitatively later on in Fig. 8. A rudimentary oxygen-depletion region appears near the spacecraft, and again no emission from the region rearward of the exhaust plane is detectable. Luminosity begins to extend outside the camera field as early as 1 s, in an unsymmetric pattern that does not lend itself to extrapolation; nonetheless this radiating region also gives the impression of reaching an essentially steady state in the orbiter's moving reference frame at that time.

Wake-Directed Exhaust

The much weaker wake glow (Fig. 2d) similarly becomes stable by about 1 s. This volume appears to be a hollowed ogive or quasi-cone, with an initial half apex angle somewhat larger than the 23-deg final expansion-cone angle of the PRCS nozzles. Its projections resolve no gap in visible surface brightness extending from the exit plane, but when the radiating volume reaches a steady state, its total emission per unit axial length—i.e., the station radiance—decreases steeply toward the nozzles in the initial retrograde ~1.5 km. Again no emission from the hemisphere opposite to exhaust injection is above camera threshold.

An interpretation that the limb enhancement arises from the excess liquid fuel flowed to cool combustion-chamber walls would be consistent with excitative reactions of MMH products with the background atmosphere. This brightening, however, must also be in part due to the increased concentrations of $O(^3P)$ reactant near the periphery of the exhaust flow, associated with decreases toward its symmetry axis. The initial upstream growth of station radiance noted just above would again be due to the exhaust gas encountering nearer-ambient densities of oxygen atoms. The frames after thruster shutdown show the spacecraft moving away from the still-luminescing interaction volume, illustrating the expected drag of the orbital atmosphere on its reactive (and/or metastable) species.

Radiance Profiles and Growth Velocities

We extracted axial and perpendicular-to-track brightness profiles from the images in Fig. 2a (STS-56, April 19, 1993), from which characteristic dimensions could be defined and volume emission and total-yield rates derived. (The traces were corrected for the small change in plate scale during the measurement period.) In the earlier-acquired video sequence reproduced in Fig. 2b (STS-33, Nov. 24, 1989) the projection of the radiating volume overfills the camera field in both directions about 0.5 s before its growth slows dramatically; nevertheless, unlike the generally higher-quality STS-56 images, this record contains information about persistence of the emission. The unsymmetric and likewise incompletely imaged patterns from a cross-track exhaust injection (Fig. 2c) are not amenable to description by a few numerical parameters. The weaker wake glow (Fig. 2d), which also soon extends beyond the camera field, provides much lower signal/noise ratio and thus less reliable dimensions and photon yields.

Ram Glows

Figure 3 shows axial profiles during the initial rapid expansion of the STS-56 luminous volumes. We define the intercepts on the dark-current baseline of the straight lines manually fitted to their downstream sides (in Fig. 3) as fronts of the exhaust interaction. Figure 4 is a plot of these front positions relative to the spacecraft, which is readily located in virtually all frames. (Its position in fact drifts only a few pixels during the measurement period, showing the tracking precision to be ≲1″.) Comparison between SWIR and visible front locations thus extracted from the continuous-tone photographs is justified by 1) the comparable dynamic ranges of these image data and 2) the observation that the ratio of axial velocities of the directly identifiable maximum-brightness positions is very near the corresponding ratio for these brightness fronts. Uncertainties in velocity of advance stated in Fig. 4 represent one standard deviation from best-fit straight lines, without consideration of systematic photogrammetry error; model refers to results of the SOCRATES code[19] calculations discussed below.

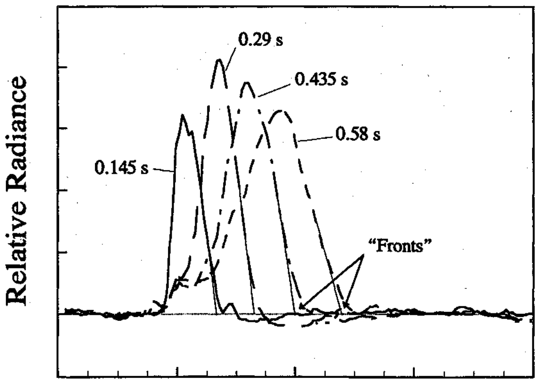

a) Visible

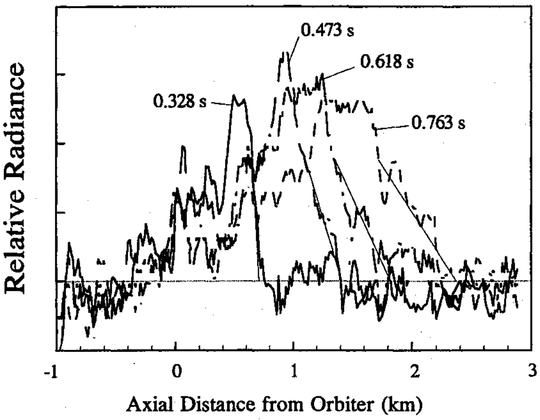

b) SWIR

Fig. 3 Axial radiance traces through the STS-56 interaction volumes.

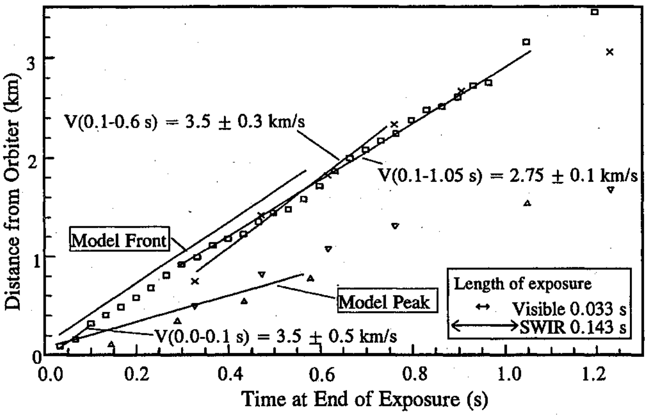

Fig. 4 Axial positions of the peaks and fronts of the STS-56 SWIR and visible interaction glows: △, visible peak; ▽, SWIR peak; □, visible front; and ×, SWIR front.

Similar cross-track traces through the positions of maximum surface radiance are in Fig. 5. The insert shows the SWIR camera data fit to a Gaussian. Distances from the spacecraft to these column

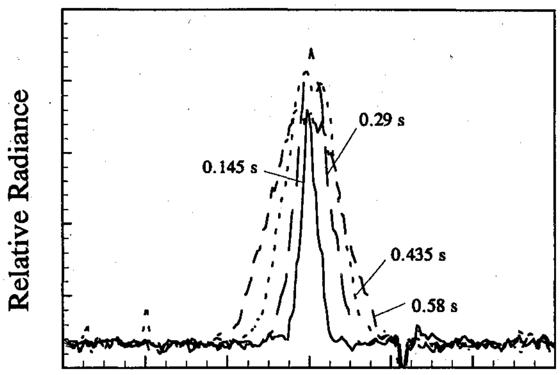

a) Visible

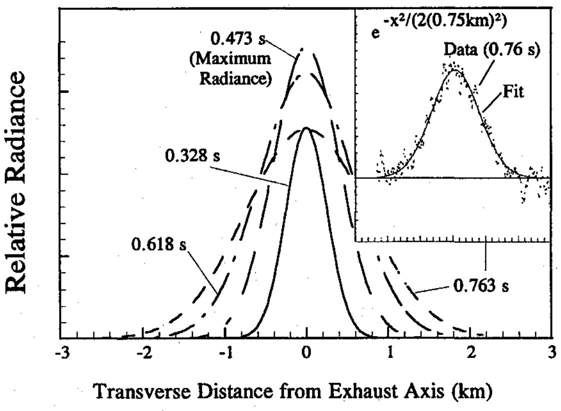

b) SWIR

Fig. 5 Transverse radiance profiles through the maxima of the STS-56 glows.

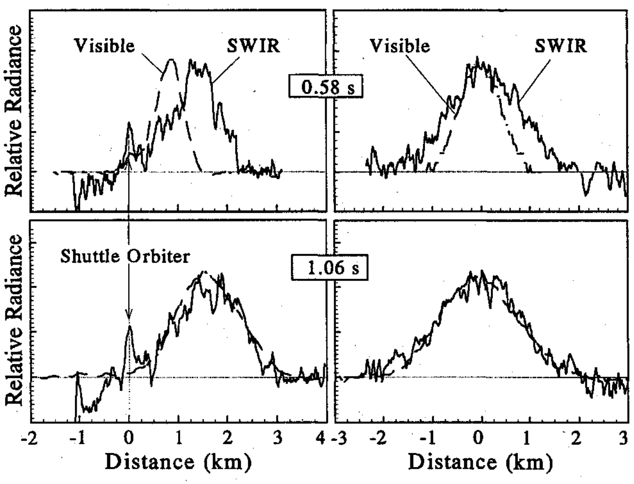

Axial from orbiter
Transverse through maximum

Fig. 6 Radiance profiles at two times after STS-56 PRCS ignition.

emission-rate maxima have no particular physical meaning, other than that they locate the volume-emission-rate maxima fairly reliably. The SWIR radiance maximum and front move to windward significantly more rapidly than the visible during this initial 0.6 s, and the SWIR spatial distributions then are also broader both axially and transversely. The posigrade velocities of the SWIR glow volume are decreasing, so that the two profiles overlie one another by about 1 s (within the resolution of these image data; see Fig. 6). That this difference in growth rates at early times is not merely an effect of our definition of the radiance fronts is to some extent further evidenced by the downstream bulge in the SWIR isophote plots in Fig. 2a.

These profiles transverse to the orbital track through the radiance maxima make reasonably satisfactory fits to a Gaussian functional form. We adopt the standard width parameter, implicitly defined in the lower panel of Fig. 5, as the measure of dimensions of these soft-edged luminescing regions. Data points were assigned equal weight in the least-squares fitting. The SWIR transverse Gaussian half-widths (Fig. 7) approach an asymptote of 1.14 ± 0.16 km with a characteristic exponential time of 0.93 ± 0.22 s. The corresponding growth parameters for the S-20R wavelength interval are 1.49 ± 0.13 km and 1.41 ± 0.31 s; i.e., the visible exhaust-interaction volume becomes about 30% wider over a 50% longer period. (Uncertainties quoted here and later represent the departures from best fit at which the sum of residuals has increased by a factor 3, which corresponds roughly to 90% confidence; systematic measurement error is again not considered.)

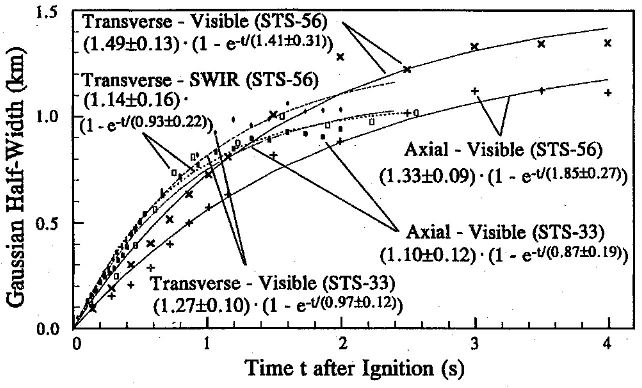

Fig. 7 Growth of the STS-56 luminous exhaust interaction volumes.

The SWIR axial profiles are too noisy and asymmetric for satisfactory application of this automatic procedure. Manual smoothing, however, allows estimation of their full widths between photocurrents in the same ratio to the maximum photocurrent as in the Gaussian definition $[(1/e)^{1/2}]$. After 1 s this dimension is 2 × (0.8 − 0.9) km. The visible-emission pattern expands more slowly, consistent with the behavior of its front, and reaches an asymptotic axial half-width of 1.33 ± 0.09 km with an exponential time of 1.85 ± 0.27 s. (The changing viewing angle from AMOS during the ≈3-s measurement period produces a small systematic error relative to the precision of these image-derived figures.) Both brightness distributions are broader in the cross-track direction; the visible is asymmetric about the transverse lines through its maximums, with less-convex contours toward the source of exhaust gas.

The <1 s of fully useful geometry data available on the STS-33 ram exhaust interaction (Fig. 2b) indicate that the similarly defined radiance front advances with a similar functional dependence on time after PRCS turn-on. Best statistical fits to the half-width asymptotes and grow-in times of the axial and transverse-to-track expansions are 1.095 ± 0.12 km, 0.87 ± 0.19 s and 1.27 ± 0.10 km, 0.97 ± 0.12 s, respectively. The apparently high precision of these figures is due to the high spatial resolution of the long-focus camera. Since the systematic error in extrapolating to beyond 1 s could be large, no significance can be ascribed to differences from the growth parameters of the visible STS-56 ram glow, which refer to background air with factor-*e*, or one scale height, higher density.

Normal-to-Trajectory and Wake Glows

Profiles through the area of maximum horizontal width of the visible luminosity from the perpendicular thruster firing are shown in Fig. 8. That the highest surface radiance remains nearly unchanged during the initial 1 s is an artifact of the selection of these traces. This area also has steeper trailing than leading edges, which is again an effect of depletion of the background reactant. The distance to the uppermost front position increases at 3.1 ± 0.4 km s^{-1} in the initial 0.7 s, which within measurement error is the initial velocity of the exhaust gas relative to the orbiter. The largest full widths parallel to the trajectory, defined as in Fig. 3, turn out to increase at sensibly the same speed.

In the initial 0.7 s of the wake firing the corresponding relative velocity of the luminosity front is 3.5 ± 0.4 km s^{-1}, again the exhaust velocity. (This uncertainty estimate takes into account systematic error in the coadded signal resulting from subthreshold radiances, which are evidenced by the photocurrent distributions in the first few video frames.) The corresponding rate of growth of the maximum full widths averages 3.4 ± 0.5 km s^{-1} over this period, after being

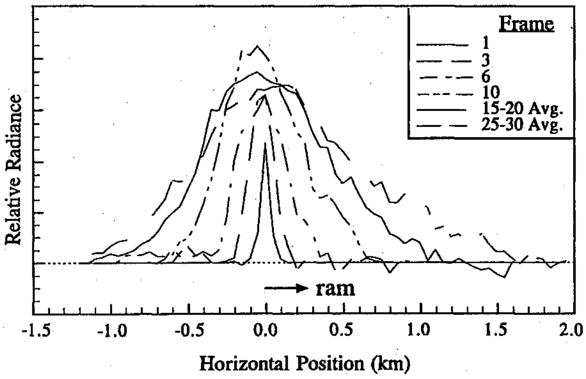

Fig. 8 Transverse profiles through the peak radiance of the STS-33 perpendicular-directed exhaust interaction volume.

somewhat larger in the initial 0.2 s. This phase velocity is (within measurement precision) the same as that of the maximum widths of the transverse-to-trajectory interaction volume; the cross-track widths of the ram glows appear to be increasing less rapidly, as are their axial-front displacements (Fig. 4). The emission per unit axial length after 1 s peaks at about 1.5 km from the spacecraft, and then decreases roughly exponentially with a characteristic distance of 2.8 ± 0.4 km.

Radiant Intensities

STS-56 Measurement

Figure 9 is a plot of the total transmitted power from the STS-56 ram volume in the two wavelength intervals. The relative SWIR yield rates were accessed by summing the photocurrents above the baseline (leakage) currents from the photodetector array, which we measured pixel by pixel just before the PRCS engines ignited. In the visible-light images, irradiance streaks from stars and out-of-frame glow introduce unacceptable error in such automatic integrations; we therefore determined the total yields making use of the Gaussian widths plotted in Fig. 7.

The SWIR power outputs can be seen to approach an asymptote about exponentially. Weighted by their magnitudes, as is justified by the increasing uncertainty in signal photocurrent toward the dark baseline, they best fit a characteristic growth period 0.41 ± 0.06 s. The visible power outputs, in contrast, initially exhibit distinct upward rather than downward curvature, heuristically fitting the functional forms in Fig. 9.

Interpretation

An exponential dependence of total light output on time after injection of exhaust gases begins would result from a constant fractional rate of their at least in part chemiluminescence-producing consumption. That is, the observed behavior of SWIR emission indicates that its rate-limiting step is that of a first-order reaction of one or more combustion-product species (input at a constant rate, as from the PRCS engines) with the atmosphere's atoms or molecules (essentially undepleted within the volume encompassed by the camera's field). The characteristic grow-in period can thus be directly interpreted as the inverse of the product (spatially averaged concentration of ambient reactant) × [available-energy-averaged rate coefficient of the reaction (or elastic collision) that removes (or reduces below reaction threshold the translational energy of) exhaust species].

By contrast, the initial upward curvature of power output in visible photons is characteristic of chemical processes involving formation of an intermediate, or alternatively, consumption of some competing species in the reaction volume. These yield rates make satisfactory fits to the functional form $1 - \exp[-(t/\tau_3)^2]$, which approaches $(t/\tau_3)^2$ when $t < \tau_3$. (The τ_i are given in Fig. 9.) They also fit

$$\tau_2[1-\exp(-t/\tau_2)]-\left(\tau_2^{-1}-\tau_1^{-1}\right)^{-1}[\exp(-t/\tau_1)-\exp(-t/\tau_2)] \quad (6)$$

which has more physical significance as it would result from the following two-step process.

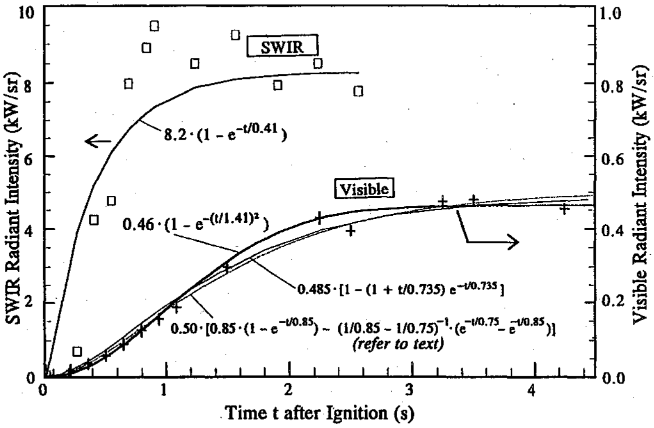

Fig. 9 Total radiant intensities from the STS-56 exhaust interaction volumes.

One or more exhaust species (again input at a constant rate) reacts as described in the preceding to increase the number of precursor molecules or atoms:

$$A = c_A \tau_1 [1 - \exp(-t/\tau_1)] \quad (7)$$

Species A concurrently participates in reactions (again with the chemically or dynamically undepleted ambient atoms and/or molecules) that produce excited species B at a comparable fractional rate:

$$\frac{\mathrm{d}B}{B\mathrm{d}t} = \frac{c_B A}{B} - \frac{B}{\tau_2} \quad (8)$$

B then radiates in a time short compared with the scale of this chemistry. The constants c_A and c_B normalize the total number of reactions within the volume viewed by the cameras, and τ_1 and τ_2 are the inverse fractional step rates, i.e., characteristic times. The solution of Eq. (8) is

$$B = c_A c_B \tau_1 \times \text{[the expression in Eq. (6)]} \quad (9)$$

In the special case that these two reaction times are equal ($\tau_1 = \tau_2 \equiv \tau$), the photon output rate becomes

$$c_A c_B \tau \times \{\tau[1 - \exp(-t/\tau)] - t\exp(-t/\tau)\} \quad (10)$$

Figure 9 shows the visible radiant intensities also to be fitted satisfactorily with a single characteristic time (0.73_5 s), which means that the above-mentioned product of total number of reaction partners and rate coefficient is sensibly the same for each of the two steps. If this ambient reactant were the same species, the two rate coefficients would be equal. Furthermore, with the extremely plausible assumption that it is due to $O(^3P)$ at the average density of 10^9 cm^{-3} typical of the orbiter's operation altitude, this coefficient would be about 1.5×10^{-9} cm^3/s. To the extent that a cross section can be reliably extracted from a single rate datum, the cross section for the reactions resulting in visible luminosity would be closely 1.5×10^{-15} cm^2, or geometric.[46,47] (N_2, with almost order-of-magnitude-lower density, could not be the dominant reaction partner, as it would call for an unrealistically high cross section.)

STS-33 Measurements of Growth and Decay

The radiant intensities from this ram-directed firing (in Fig. 2b) evidence a similar upward curvature in the initial 0.7 s for which good data are available.[42] They fit the yield rate expression for equal characteristic reaction times [(Eq. 10)] with $\tau = 0.47 \pm 0.03$ s and an asymptotic power output in the S-20R interval of 0.34 ± 0.03 kW/sr. (These best statistical fits are sensibly the same when the surface brightnesses are weighted equally and by their magnitudes.) Although this growth period is about $\frac{1}{3}$ shorter than that derived from the longer-duration STS-56 data set, the optical power outputs reached (see Fig. 9) are the same within the estimated error of the intensified-video photometry.

Similarly, a plot of visible radiant intensities from the perpendicular firing (in Fig. 2c) is somewhat concave upward before 0.4 s and then flattens out over the next 0.2 s. (Too much of the emitting volume lies outside the camera's field for us to quantify their later behavior.) The best-fit τ is 0.76 ± 0.08 s. These small fractional statistical uncertainties are again an effect of the camera plate scale for the STS-33 images; truncation of the data and other experiment inaccuracies lead to a significantly larger inherent error range.

The total yields of visible light from the wake firing (in Fig. 2d) have an essentially constant rate of increase in the initial 0.5 s. That is, no curvature is evidenced by the noisy plot of the sums of photocurrent over baseline. This observation may be interpreted as showing that the reactions of the exhaust component(s) responsible for these AMOS images are taking place on a scale long compared with 0.5 s.

Solution of Eq. (8) for after thruster shutoff shows that as τ_2 approaches τ_1 the decrease of radiant intensity becomes closely exponential, with this characteristic time. We summed the projected-column emission rates in Fig. 2b over rectangular areas extending 2.2 km into ram and 2 × 0.34 km in the perpendicular (near-vertical) direction from orbiter. The yield rates from these limited segments decay exponentially, with characteristic time 1.25 ± 0.1 s between ~0.5 and 4.5 s after injection of exhaust ends.[42] Since the tracked body is moving, albeit slowly, into the excited gas,[6] the reciprocal of this period represents a lower limit to the fractional rate of decrease of total power output in visible photons. (The fraction of STS-33 wake glow remaining within the camera's field after shutoff is too uncertain to allow reliable estimation of decay periods for this exhaust direction.)

We similarly reduced images of a 240-ms-duration firing[42] of PRCS engines into the windward hemisphere from STS-29 (333 km, March 17, 1989), obtained by an AMOS video camera whose $\frac{1}{20}$-rad field of view encompassed all of the luminous region. This data set also showed a closely exponential falloff of radiant intensities, with a decay period (0.9 ± 0.1 s) somewhat shorter than that extracted from the incomplete STS-33 ram images.

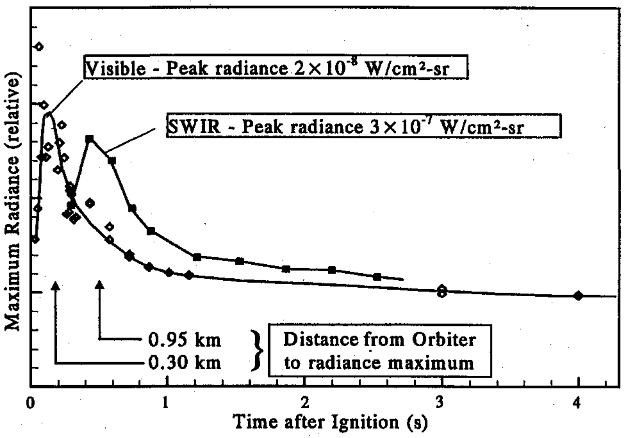

Fig. 10 Peak surface radiances of the STS-56 exhaust interaction volumes.

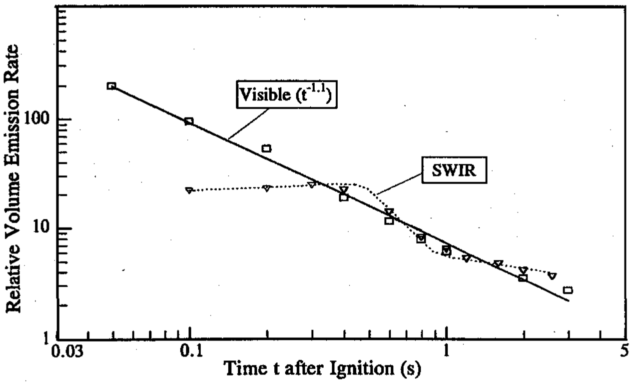

Fig. 11 Relative central volume emission rates in the STS-56 interaction glow (scaled for comparison of time dependences).

Optical Yields

Figure 9 shows that when the STS-56 interaction reaches a near-steady state, the total rate of production of SWIR-band radiation that would be transmitted to AMOS is 100 kW. This yield is equivalent to one photon per nine MMH-fuel molecules consumed, or roughly 1% of the engines' thrust power. The actual exoatmospheric output in this spectrum interval is significantly larger, as will become evident when we estimate below the attenuation of candidate rovibrational features along the slant view path.

The corresponding number of S-20R-interval photons is 1 per 1000 MMH molecules, or <1% of the number of vibrational photons. Although scattering and absorption in the visible are both small and (unlike SWIR) only weakly dependent on wavelength, this yield has an estimated ±50% inherent error due to uncertainty in the exposing spectral distribution.

The ratio of power output within the two STS-56 wavelength intervals varies with time after ignition as indicated in Fig. 9. Extrapolation of the STS-33 radiant intensities when the interaction volumes remained confined to the video camera's field (from Figs. 2b–d) leads to an estimate[1,42] of ram:perpendicular:wake ≈ 60:30:1 after 2 s. This ratio is of course also changing during the initial unsteady exhaust flow.

Volume Emission Rates

The maximum radiances of the STS-56 glow (Fig. 10) peak before 0.5 s and decrease slowly during the slower-expansion period beyond 1 s. A similar, but less pronounced, early maximum is observed in the STS-33 ram exhaust interaction.[42] The mean radiances in the S-20R wavelength range are very much higher than those reported[6] for the O I forbidden red lines, which shows—or at a minimum very strongly suggests—that this nominally directly excited spectrum feature[6] represents only a small part of the visible-range image signal.

The interaction region can be readily shown to reabsorb a negligible fraction of the candidate infrared radiations considered in the next section, and would be optically thin to visible-range molecular bands also. Volume emission rate distributions that result in Gaussian surface radiance profiles of cylindrically symmetric such glows are also Gaussian, with the same width parameter. Figure 11 is a plot of the central volume emission rates extracted from these maximum brightnesses and the best-fit (i.e., smoothed) maximum transverse widths of the STS-56 glows in Fig. 7. These volume emission rates refer to the outward-moving axial locations of these peaks shown in Fig. 4, rather than some fixed posigrade distance from orbiter. In practice, they could be as much as 25% higher elsewhere within the luminous volume, as their values in our definition are strictly speaking maxima only when this region is spherically symmetric.

This local power output in electronic emissions can be seen to decrease by almost two orders of magnitude after the first useful video frames. The corresponding relative change in volume rate of emission of rovibrational bands is definitely smaller, which is in the direction expected when luminescence results from a single-step reaction with the (depleted) atmosphere. (The about constant-appearing SWIR data points before 0.3 s are extrapolated from Figs. 7 and 10 and thus are less reliable than the data for later times.) This central visible-interval volume emission rate varies roughly as t^{-1} in the initial 1 s. Such a dependence would result from the linear growth of the radiating volume in each dimension combined with the aforementioned square-law increase in total output power that fits a chain of two reactions with comparable rates when $t < \tau$; that is, it follows from $t^{-3} \times t^2$. This simple empirical argument is less applicable to the SWIR, where the measurements of yield rates and effective dimensions are sparse and uncertain during the brief initial period when $1 - \exp(-t/\tau)$ can be approximated as t/τ. Nonetheless, the SWIR data points between 0.4 and 1 s do give some suggestion of the expected dependence on $t^{-3} \times t^1 = t^{-2}$.

Exoatmospheric Emission Yields

Excitation and attenuation by the atmosphere of rovibrational bands potentially responsible for SWIR from ram-directed exhaust interactions were estimated[48] by applying an adaptation of the SOCRATES Monte Carlo model,[19] which numerically treats unsteady reactive flows in the transitional-flow[33] regime. The inelastic cross sections and internal temperatures applied are largely based on recent measurements,[15–18] with some further input from older sources.[14,32,44,45,47] (Particulars of the reanalysis of the recent laboratory data on radiations from hypervelocity H_2O–O collisions are presented separately.)

Dependence on Time after Turn-On

The calculated SWIR radiant intensities from each of the neutral-atom-interchange and nonreactive processes [Eqs. (1) and (3–5)] grew into asymptotes with characteristic exponential times within 30% of the 0.4 s observed; the fronts moved to windward, as shown in Fig. 4. The density of undisturbed background air is near 10^9 cm^{-3}, and cross sections for elastic collisions of the closely 10^6-cm s^{-1}-relative-velocity combustion species are of order 2×10^{-15} cm^2. Thus this period this may be interpreted as the mean time to this first collision [$(10^9 \times 10^6 \times 2 \times 10^{-15})^{-1}$ s], which has the effect of reducing the kinetic energy below thresholds for exciting vibrational states.

This interpretation is also consistent with the approximately 2-km axial dimension of the radiating ram volume after 1 s. The spatial distribution of SWIR glow is thus largely determined by elastic collisions, which is not surprising in that their cross sections are at least an order of magnitude higher than those for internal excitations (with the exception of H_2O ν_2), or atom interchange. [In this regard, its time dependence shows that the aforementioned reactions of H_2O and H_2 with O(^1D) that may be produced in the interaction volume do not contribute significantly to the SWIR signal.]

Transmission by the Atmosphere

Absorption of these infrared radiations along the path to AMOS was calculated line by line,[48] using a nonequilibrium spectral model that approximates the distributions of levels for each vibrational mode and rotation by individual temperatures. The spectral distributions for H_2O were based, with the important modification noted in the next paragraph, on the classical theoretical cross sections for its excitation[32] in several-electron-volt collisions with O. (N_2 has a very much lower probability of exciting H_2O stretch modes.[14]) Doppler shifts due to the radially directed velocities of the interaction volume were calculated to have only negligible effect on transmission of its water-molecule bands through the cooler water vapor of the lower atmosphere. The temperatures for OH were based on a reanalysis, to be briefly outlined in the following paragraphs, of spectra from recent hypervelocity oxygen-atom beam experiments[11,17]; those for CO came from fits to the optical data from an on-orbit gas release.[18]

A separate calculation[48] based on a classical model of rotational cascade[49] showed that the effective rotational temperature for the 0.2-s-lifetime H_2O 100 → 000 (ν_1) transition would be substantially reduced (to near 1000 K) by radiative relaxation of the higher-lying rotational states. Similarly, the ν_2 vibrational band(s) would be so cooled that only a negligible fraction would extend down to the infrared camera's response wavelengths. The absence of identifiable bending-mode emission from H_2O^+ in the spectra of outgassed water[37] indicates that the even less readily excited stretch-mode radiations of this molecule are also not contributing to the SWIR signal; therefore no calculation of their attenuation was indicated.

The effective transmissions to the image plane thus derived are 0.4 for the OH $\Delta v = 1$ sequence excited by atom transfer from H_2O [Eq. (1c)], 0.2 for the CO $\Delta v = 2$ sequence, and 0.2 and 0.2_5, respectively, for the overlapping H_2O ν_1 and ν_3 bands. That is, the infrared camera's current outputs per photon/s from each of the primary-candidate exoatmospheric processes lie within a range of a factor 2. (Code runs with a different water-vapor profile showed little change in these band transmissions.[48])

CO/CO_2, N_2, H_2

Reactions of these principal exhaust components [Eqs. (3–5)] were found on further investigation to make only small contributions to the large steady-state infrared yields measured. The cross sections[15,18] for production of CO ($X, v \geq 2$) at 8 km/s relative to elastic scattering, along with the <10% branching into its overtone, lead to less than 1% of the observed signal; in consequence, an unrealistic increase in these excitative cross sections of at least a factor 100 between velocities of 8 and 8 + 3.5 km s^{-1} would be required for the reactions (3) to become significant. Similarly, applying the upper-limit atom-exchange cross section inferred from an N_2 gas release[18] for the reaction (4) would result in only a very small fraction of the SWIR photons (hence no transmission calculation was made for the NO overtone).

The reaction (5) leading to OH ($X, v = 1$) has been shown theoretically[39–41] to proceed only when the (hypervelocity) hydrogen molecule is vibrationally excited. With the highly questionable assumption that the 3200-K temperature of the PRCS combustion chamber is frozen in to the vibrational distribution of exhaust H_2, these calculated state-to-state cross sections would result in about 10% of the observed SWIR yield.

H_2O

Broadband spectra from laboratory bombardment of water vapor by 8 ± 1-km s^{-1} oxygen atoms[11,17] showed emission between 1.3 and 2.0 μm, comparable with that in a peak extending from about 2.6 to 3.7 μm. The wavelength distribution, corrected for transport out of the sensor's field of view before radiative decay, can be fitted by hydroxyl with 7000 ± 1000-K vibrational and 1500 ± 200-K rotational temperatures.[48] This (as yet unverified) observation of emission shortward of 2 μm is a major factor in favoring the atom-exchange reaction of H_2O with O as the principal source of the longer-wavelength radiation imaged by the infrared camera. Relatively high transmission of the OH fundamental sequence to AMOS is a qualitatively supporting consideration, as it results in a more plausible (lower) yield of SWIR photons than would the H_2O stretch bands.

Direct impact excitation of water molecules [Eq. (1a)] would not satisfactorily explain the laboratory spectrum. If a major fraction of the shorter-wavelength peak were a result of their multimode transitions (in particular 110 and 011 → 000 near 1.9 μm), their single-quantum stretch bands above ≈2.5 μm (001 and 100 → 000) would have been far more intense. In addition, the spectral extent of the longer-wavelength peak is less consistent with the rotationally relaxed H_2O stretch distribution predicted than with the fundamental sequence from OH that would accompany its first overtone.

The aforementioned vibrational temperature, if it applies to all upper states, would result in too little red–yellow higher-overtone (4–0, 5–1, and 5–0, ...) hydroxyl emission to affect significantly the visible-band AMOS images. This observation is borne out by both the ground-based spectra[6] and the measured time dependence of visible yield rates. OH at these fitted temperatures would lead to 1 SWIR photon emitted per 3 (±1.5) MMH fuel molecules consumed, or per 6 (±3) H_2O molecules exhausted. The latter figure follows from an optical cross section somewhat above 10^{-16} cm^2 at 5.8-eV mean rest-frame energy; vibrational cascade would lead to a mean excitative reaction cross section for the reaction (1c) roughly a factor two smaller, or an order of magnitude below the cross section for elastic scattering of H_2O by O.

Discussion

A principal finding from these images of the diffusive expansion of windward-directed PRCS exhaust gases is that rovibrational emission is directly excited in single collisions with background air while the visible electronic emissions detected involve an intermediate reaction. This first step proceeds with a rate coefficient very near that of the chemiluminescent reaction(s), and gives strong evidence of involving the same ambient species, atomic oxygen. That the visible ram glow volume becomes larger than the SWIR after the initial ~1 s of near-injection-velocity growths is consistent with such a difference between the orders of the excitation processes, as its precursor species would be diffusing outward. The component of forbidden red oxygen-atom lines directly excited[6] is not sufficiently strong to affect the time dependence of visible radiant intensities, within their precision of measurement by the AMOS tracking camera. As excitation cross sections derived from the grow-in (and decay) times of these output rates are close to geometric, only an unrealistically large rate coefficient could have obscured an intermediate step in populating upper states of the vibrational transitions.

The exoatmospheric yields of 2.3–3.6-μm photons from ram interactions depend on the rotational development of vibrational bands whose optical cross sections at hyperthermal impact velocities are not well understood. Primarily recently available input information was applied in preliminary model calculations of the irradiances that would be transmitted to the mountaintop observatory in energetically allowed, high-branching-ratio molecular band systems.[48] The $\Delta v = 1$ sequence of OH ($X^2\Pi$) emerges as the most plausible dominant source of the SWIR camera signal at closely 5.75-eV center-of-mass kinetic energy. [At the $\approx$ 3 eV of outgas, the reaction (1c) appears to be producing few hydroxyl radicals in high rotational states.[37]] Application of its expected spectral distribution leads to an estimate of one such photon emitted per three fuel molecules consumed when ram PRCS exhaust interactions attain a quasisteady state, and a physically reasonable magnitude of the absolute cross sections for the excitative atom-exchange reaction (1c).

Outgassed H_2O has also been found to become collisionally excited; thus fundamental cross-section and internal-state distribution data could be obtained from onboard spectroradiometry of water released in low orbit. (Routine liquid ventings from the Space Shuttle, for example, result in some two orders of magnitude higher column densities of vapor than its mean outgas.) Measurement in the hydroxyl first overtone sequence from exhaust interactions would be particularly effective in determining yields in OH fundamental bands, as well as for assessing the part played by the reaction (5). Such spectra would be readily interpretable, as the lower atmosphere is relatively transparent in the near IR (but unfortunately bright at OH-rotation wavelengths). In this regard, high-resolution (4 cm^{-1}) spectra of the natural OH $\Delta v = 2$ nightglow with roughly two orders of magnitude lower radiance can be obtained in ~100 s with sensors of modest light grasp,[50] so that achieving a similar signal/noise ratio from AMOS on the ~0.5-s time scale of exhaust interactions should present little experimental difficulty.

The corresponding number of visible-range photons from ram glows, which depends much less strongly on modeling of exoatmospheric yields and atmosphere transmissions, is 0.001 per MMH molecule. This low figure supports the previous inference that most of this radiation has its origin in the 10^{-3}–10^{-2} fraction of directly exhausted labile fuel and product species associated with the variable mixing ratios and temperature[8] within PRCS combustion chambers. The kinetic complexity apparent in the AMOS video data is consistent with chemiluminescence originating from minor rather than direct excitative atom interchange and nonadiabatic collisions of major exhaust components.[1,43]

The decrease in visible radiant intensity with increasing angle between the combustion-gas stream and the spacecraft trajectory can be interpreted as due to a potential barrier for (at least) the first reaction step.[1] This readily measured, time-dependent total emission rate and the radiance patterns from which it is derived (Fig. 2) are principal elements of the optical signature of liquid-bipropellant thruster firings. These observables serve as a basis for remote sensing of this angle (as well as thrust assessment) for tracking and surveillance of space vehicles powered or oriented by rocket motors of similar design.

As the visible-range and SWIR transverse-column emission rates are symmetric about the thrust axis in direct ram and wake injections, straightforward unfolds extract volume emission rates, which are the more fundamental physical quantities. (No radiation from the hemisphere rearward of operating thrusters is detectable in the AMOS images.) Beyond 1 s the maximum ram volume emission rates become smaller by two orders of magnitude in the visible and more than one order of magnitude in the SWIR than the highest earlier maxima, in accord with the reduction in densities of the oxygen-atom reaction partner predicted by explosion-dynamics theory.[4,5]

Conclusions

Computational models of the exhaust and background gas densities, applied with these measured volume emission rates, would result in improved rate coefficients for the infrared and visible luminosity-producing (or particle energy-degrading) processes. Future PRCS firings to refine the measurements reported here need extend over only the $\approx$2 s in which the interactions from all exhaust directions come to essentially steady states; images encompassing previously disturbed air over a somewhat longer period after precisely known thrust turnoff would provide further reaction-kinetics and species-transport data. Our analysis of the data available shows that passive remote sensing of both the visible and infrared emissions locates the high-relative-translational-energy component of the flowfields.

Quite obviously, spectra (preferably space-resolved), complemented by photographs in defined wavelength intervals, are needed to identify the emitters and determine how they are being excited. This information would allow scaling of the contaminating optical foregrounds/backgrounds from spacecraft effluents to further flight altitudes and spectrum regions. Radiances in the $\approx$1.3–1.7-μm overtone bands of hydroxyl would be particularly effective in assessing the relative contributions from OH and H_2O (and reactions of exhaust H_2) to the $\approx$2.5–3.5-μm SWIR emission.

Acknowledgments

The authors thank the staff of Visidyne, Inc. (Burlington, MA), who were responsible for the infrared imager; of AMOS, who operated the precisely tracking video cameras; of the University of Arizona's Lunar and Planetary Observatory, who constructed and calibrated the imaging spectrograph; and of the Shuttle orbiter, who controlled operation of the PRCS thrusters. Extremely valuable theoretical and interpretive contributions were made by L. S. Bernstein and J. B. Elgin of Spectral Sciences, Inc. (Burlington, MA). These include the calculations of the atmosphere's transmission of candidate short-wavelength infrared bands, reanalysis of laboratory measurements that apply to the reactions (1) with derivation of effective radiating temperatures, calculation of the rotational relaxation of H_2O before vibrational emission, and an initial model of the two-sequential-step reactions that result in visible luminescence. The AMOS infrared camera (model AE4128C) was provided by Amber Engineering, Goleta, CA, and the visible-sensitive photocathode by Pulnix, Sunnyvale, CA. We thank also R. E. Meyerott (Lockheed Martin Palo Alto Research Laboratory), P. J. McNicholl and R. B. Garner (PhotoMetrics), and R. A. Viereck and E. Murad (U.S. Air Force Phillips Laboratory/WSAI) for stimulating discussions.

References

[1] Murad, E., Knecht, D. J., Viereck, R. A., Pike, C. P., Kofsky, I. L., Trowbridge, C. A., Rall, D. L. A., Ashley, G., Twist, L., Elgin, J. B., Setayesh, A., Stair, A. T., Jr., and Blaha, J. E., "Visible Light Emission Excited by Interaction of Space Shuttle Exhaust with the Atmosphere," *Geophysical Research Letters*, Vol. 17, No. 12, 1990, pp. 2205–2208.

[2] Bernhardt, P. A., "High Altitude Gas Releases: Transition from Collisionless Flow to Diffusive Flow in a Non-Uniform Atmosphere," *Journal of Geophysical Research*, Vol. 84, No. 8, 1979, pp. 4341–4354.

[3] Brode, H. L., and Enstrom, J. E., "Analysis of Gas Expansion in a Rarefied Atmosphere," *Physics of Fluids*, Vol. 15, No. 11, 1972, pp. 1913–1917.

[4] Groves, G. V., "Initial Expansion to Ambient Pressure of Chemical Explosive Releases in the Upper Atmosphere," *Journal of Geophysical Research*, Vol. 68, No. 10, 1963, pp. 3033–3047.

[5] Bernhardt, P. A., Kashiwa, B. A., Tepley, C. A., and Noble, S. T., "Spacelab 2 Upper Atmosphere Modification Experiment over Arecibo, 1, Neutral Gas Dynamics," *Astrophysical Letters and Communications*, Vol. 27, No. 3, 1988, pp. 169–182.

[6] Broadfoot, A. L., Anderson, E., Sherard, P., Knecht, D. J., Viereck, R. A., Pike, C. P., Murad, E., Elgin, J. E., Bernstein, L. S., Kofsky, I. L., Rall, D. L. A., Blaha, J., and Culbertson, F. L., "Spectrographic Observations at Wavelengths Near 630 nm of the Interaction Between the Atmosphere and the Space Shuttle Exhaust," *Journal of Geophysical Research*, Vol. 97, No. A12, 1992, pp. 19501–19508.

[7] Rall, D. L. A., Gardner, J. A., and Kofsky, I. L., "Analysis of Images of Spacecraft Thruster Induced Radiations," PL-TR-94-2209, U.S. Air Force Phillips Lab., July 1994.

[8] Viereck, R. A., Bernstein, L. S., Mende, S. B., Murad, E., Swenson, G. R., and Pike, C. P., "Visible Spectra of Thruster Plumes from the Space Shuttle Primary Reaction Control System," *Journal of Spacecraft and Rockets*, Vol. 30, No. 6, 1993, pp. 724–730.

[9] Dressler, R. A., and Murad, E., "Ion Chemistry in the Spacecraft Environment," *Unimolecular and Bimolecular Reaction Dynamics*, edited by C.-Y. Ng, T. Baer, and I. Powis, 1st ed., Wiley, London, 1994, pp. 88–182.

[10] Heninger, M., Fenistein, S., Mauclair, G., Marx, R., and Murad, E., "Review of the Reaction of O^+ and H_2O and Its Bearing on Composition Measurements from the Space Shuttle," *Geophysical Research Letters*, Vol. 16, No. 2, 1989, pp. 139–141.

[11] Meyerott, R. E., Swenson, G. R., Schweitzer, E. L., and Koch, D. G., "Excitation of Low Lying Vibrational Levels of H_2O by $O(^3P)$ as Measured on Spacelab 2," *Journal of Geophysical Research*, Vol. 99, No. A9, 1994, pp. 17,559–17,575.

[12] Orient, O. J., Martus, K. E., Chutjian, A., and Murad, E., "Optical Emission Generated by Collisions of 5 eV $O(^3P)$ Atoms with Surface-Adsorbed Hydrazine," *Journal of Chemical Physics*, Vol. 96, No. 6, 1992, pp. 4111–4117.

[13] Orient, O. J., Chutjian, A., Martus, K. E., and Murad, E., "Observation of CN $A \rightarrow X$ and $B \rightarrow X$ Emissions in Gas-Phase Collisions of Fast $O(^3P)$ Atoms with HCN," *Journal of Chemical Physics*, Vol. 96, No. 1, 1992, pp. 427–431.

[14] Dunn, M. G., Skinner, G. T., and Treanor, C. E., "Infrared Radiation from H_2O, CO_2, or NH_3 Collisionally Excited by N_2, O, or Ar," *AIAA Journal*, Vol. 13, No. 6, 1975, pp. 803–812.

[15] Upschulte, B. L., and Caledonia, G. E., "Laboratory Measurements of IR Excitation Cross-Sections of Fast O-Atom Collisions with CO, CO_2, and CH_4," *Journal of Chemical Physics*, Vol. 96, No. 3, 1992, pp. 2025–2033.

[16] Oakes, D. B., Sonnenfruh, D. M., Caledonia, G. E., and Blumberg, W. A. M., "Velocity Dependent O Atom IR Excitation Cross-Sections—Connections with Flight Data," *Journal of Geophysical Research*, Vol. 99, No. A12, 1994, pp. 23,249–23,255.

[17] Upschulte, B. L., Oakes, D. B., and Caledonia, G. E., private communication, Physical Sciences, Inc., 1991.

[18] Green, B. D., Holtzclaw, K. W., Joshi, P. B., and Burke, H. K., "Analysis of Radiances from Orbital Gas Releases," *Journal of Geophysical Research*, Vol. 97, No. 8, 1992, pp. 12,161–12,172.

[19] Elgin, J. B., Cooke, D. C., Tautz, M. F., and Murad, E., "Modeling of Atmospherically Induced Gas Phase Optical Contamination from Orbiting Spacecraft," *Journal of Geophysical Research*, Vol. 95, No. A8, 1990, pp. 12,197–12,208.

[20] Anon., "AMOS User's Manual," rev. 7, Avco Corp., AERLM 1175, Everett, MA, 1989.

[21] Broadfoot, A. L., Sandel, B. R., Knecht, D., Viereck, R., and Murad, E., "Panchromatic Spectrograph with Supporting Monochromatic Imagers," *Applied Optics*, Vol. 31, No. 16, 1992, pp. 3083–3096.

[22] Kofsky, I. L., Rall, D. L. A., Maris, M. A., Tran, N. H., Murad, E., Pike, C. P., Knecht, D. J., Viereck, R. A., Stair, A. T., Jr., and Setayesh, A., "Phenomenology of a Water Venting in Low Earth Orbit," *Acta Astronautica*, Vol. 26, No. 5, 1992, pp. 325–347.

[23] Rall, D. L. A., Kofsky, I. L., and Gardner, J. A., "Analysis of Images and Spectra of Spacecraft-Induced Radiations," U.S. Air Force Phillips Lab., PL-TR-92-2178, July 1992.

[24] Pike, C. P., Knecht, D. J., Viereck, R. A., Murad, E., Kofsky, I. L., Maris, M. A., Tran, N. H., Ashley, G., Twist, L., Gersh, M. E., Elgin, J. B., Berk, A., Stair, A. T., Jr., Bagian, J. P., and Buchli, J. F., "Release of Liquid Water from the Space Shuttle," *Geophysical Research Letters*, Vol. 17, No. 2, 1990, pp. 139–142.

[25] Warren, W. H., Jr., "Documentation for the Machine-Readable Character-Coded Version of the SkyMap Catalogue," NASA Rept. NSSDC/W DC-A-R&S, July 1981.

[26] Pickett, J. E., Murphy, G. B., Kurth, W. S., Goertz, C. K., and Shawhan, S. D., "Effects of Chemical Releases by the STS 3 Orbiter on the Ionosphere," *Journal of Geophysical Research*, Vol. 90, No. A4, 1985, pp. 3487–3497.

[27] Trinks, H., and Hoffman, R. J., "Experimental Investigation of Bipropellant Exhaust Plume Flowfield, Heating, and Contamination and Comparison with the CONTAM Computer Model Predictions," *Spacecraft Contamination: Sources and Prevention*, edited by J. A. Roux and T. D. McCay, Vol. 91, Progress in Astronautics and Aeronautics, AIAA, New York, 1984, pp. 261–292.

[28] Young, S. J., and Herm, R. R., "Model for Radiation Contamination by Outgassing from Space Platforms," *Journal of Spacecraft and Rockets*, Vol. 25, No. 6, 1988, pp. 413–419.

[29] Wulf, E., and von Zahn, U., "The Shuttle Environment: Effects of Thruster Firings on Gas Density and Composition in the Payload Bay," *Journal of Geophysical Research*, Vol. 91, No. A3, 1986, pp. 3270–3278.

[30] Gardner, J. A., II, Rall, D. L. A., Trowbridge, C. A., Kofsky, I. L., Viereck, R. A., Murad, E., Pike, C. P., Stair, A. T., Jr., and Setayesh, A., "Optical Properties of Water Released in Low Earth Orbit," *Optical System Contamination: Effects, Measurement, Control III*, edited by A. Peter Glassford, *Proceedings of the SPIE*, Vol. 1754, 1992, pp. 124–135.

[31] Pervaiz, M. M., Richtsmeier, S. C., Gersh, M. E., and Bernstein, L. S., "Radiation Estimates for Collisionally Excited Outgassed Molecules," *Proceedings of the Vehicle-Environment Interactions Conference*, edited by R. E. Erlandson and C.-I. Meng, Johns Hopkins Applied Physics Lab., Laurel, MD, 1991, pp. 307–319.

[32] Redmon, M. J., Schatz, G. C., and Garrett, B. C., "Theoretical Studies of Vibrational Excitation in Collisions of $O(^3P)$ with $H_2O(^1A_1)$," *Journal of Chemical Physics*, Vol. 84, No. 2, 1986, pp. 764–773.

[33] Freeman, G. N., Crow, D. R., Malkmus, W., Wilson, K. H., Thomas, P. D., and Elgin, J. B., "Composite High Altitude Radiation Model (CHARM), Vol. I, Code Development," U.S. Air Force Aeronautics Lab., AFAL TR-87-019, Sept. 1987.

[34] Torr, M. R., and Torr, D. G., "Gas Phase Collisional Excitation of Infrared Emissions in the Vicinity of the Space Shuttle," *Geophysical Research Letters*, Vol. 15, No. 1, 1988, pp. 95–98.

[35] Koch, D. G., Fazio, G. B., Hoffman, W., Melnick, G., Rieke, G., Simpson, J., Witteborn, F., and Young, E., "Infrared Observations of Contaminants from Shuttle Flight 51-F," *Advances in Space Research*, Vol. 7, No. 5, 1987, pp. 211–223.

[36] Dean, D. A., Huppi, E. R., Smith, D. R., Nadile, R. M., and Zhou, D. K., "Space Shuttle Observations of Collisionally Excited Outgassed Water Vapor," *Geophysical Research Letters*, Vol. 21, No. 7, 1994, pp. 609–612.

[37] Zhou, D. K., Pendleton, W. R., Jr., Brigham, G. E., Steed, A. J., and Dean, D. A., "Infrared Spectral Measurements (400–2500 cm^{-1}) of Shuttle-Induced Optical Contamination," *Geophysical Research Letters*, Vol. 21, No. 7, 1994, pp. 613–616.

[38] Sharma, R. D., Gruninger, J. H., Sundberg, R. L., Duff, J. W., Bernstein, L. S., Robertson, D. C., and Healey, R. J., "Description of SHARC-2, the Strategic High-Altitude Atmosphere Radiance Code," U.S. Air Force Phillips Lab., PL-TR-91-2071, March 1991.

[39] Johnson, B. R., and Winter, N. W., "Classical Trajectory Study of the Effect of Vibrational Energy on the Reaction of Molecular Hydrogen with Atomic Oxygen," *Journal of Chemical Physics*, Vol. 66, No. 9, 1977, pp. 4116–4120.

[40] Whitlock, P. A., "Theoretical Investigations of the Energetics and Dynamics of the Reactions of $O(^3P, {}^1D) + H_2$ and $C(^1D) + H_2$," Ph.D. Thesis, Wayne State Univ., Detroit, 1976; *Dissertation Abstracts*, Vol. 3713, No. 11, 5689B, 1977.

[41] Schatz, G., "A Coupled States Distorted Wave Study of the $O(^3P) + H_2(D_2, HD, HD)$ Reaction," *Journal of Chemical Physics*, Vol. 83, No. 11, 1985, pp. 5677–5686.

[42] Kofsky, I. L., Rall, D. L. A., and Sluder, R. B., "Measurement and Interpretation of Contaminant Radiations in the Spacecraft Environment," U.S. Air Force Phillips Lab., PL-TR-91-2174, June 1991.

[43] Viereck, R. A., Murad, E., Knecht, D. J., Pike, C. P., Broadfoot, A. L., Anderson, E., Sandel, B., Bernstein, L., and Elgin, J., "Observations of Space Shuttle Plume-Atmosphere Interactions: Possible Contamination of Airglow Measurements," *EOS Supplement*, American Geophysical Union, 1994, p. 251 (Paper SA32A-6).

[44] Baulch, D. L., Drysdale, D. D., and Horne, E. G., *Evaluated Kinetic Data for High Temperature Reactions*, Vol. 1, Butterworths, London, 1973, pp. 527–588.

[45] Becker, K. H., and Bayes, D. K., "A Study of the Chemiluminescence from Oxygen Atom–Hydrazine Glows," *Journal of Physical Chemistry*, Vol. 71, No. 2, 1967, pp. 371–375.

[46] Bird, G. A., "Monte-Carlo Simulation in an Engineering Context," *Rarefied Gas Dynamics*, edited by S. S. Fisher, Vol. 74, Progress in Astronautics and Aeronautics, AIAA, New York, 1981, pp. 239–255.

[47] Elgin, J., and Bernstein, L. S., "The Theory Behind the SOCRATES Code," U.S. Air Force Phillips Lab., PL-TR-92-2206, Aug. 1992.

[48] Bernstein, L. S., and Elgin, J. B., private communication, Spectral Sciences, Inc., 1995.

[49] Elgin, J. B., "Classical Radiative Damping of Symmetric Top and Asymmetric Rotor Molecules," *Journal of Quantitative Spectroscopy and Radiation Transfer*, Vol. 17, No. 2, 1977, pp. 205–219.

[50] Espy, P. J., Huppi, R., and Manson, A., "Large-Scale, Persistent Latitude Structures in the Mesospheric Temperature During ANLC-93," *Geophysical Research Letters*, Vol. 22, No. 20, 1995, pp. 2801–2804.

I. D. Boyd
Associate Editor